Full Paper
doi.org/10.1002/chem.201904551

Bifunctional Nanoparticles

Magnetism and Afterglow United: Synthesis of Novel Double Core–Shell Eu^{2+}-Doped Bifunctional Nanoparticles

Huayna Terraschke,[a, c] Matthias Franzreb,[b] and Claudia Wickleder*[a]

Abstract: Afterglow–magnetic nanoparticles (NPs) offer enormous potential for bioimaging applications, as they can be manipulated by a magnetic field, as well as emitting light after irradiation with an excitation source, thus distinguishing themselves from fluorescent living cells. In this work, a novel double core–shell strategy is presented, uniting co-precipitation with combustion synthesis routes to combine an Fe_3O_4 magnetic core (≈15 nm) with an afterglow $SrAl_2O_4:Eu^{2+},Dy^{3+}$ outer coat (≈10 nm), and applying a SiO_2 protective middle layer (≈16 nm) to reduce the luminescence quenching caused by the Fe core ions. The resulting $Fe_3O_4@SiO_2@SrAl_2O_4:Eu^{2+},Dy^{3+}$ NPs emit green light attributed to the $4f^65d^1 \rightarrow 4f^7(^8S_{7/2})$ transition of Eu^{2+} under UV radiation and for a few seconds afterwards. This bifunctional nanocomposite can potentially be applied for the detection and separation of cells or diagnostically relevant molecules.

Introduction

Luminescent materials have been explored widely in the past few years for technological applications such as the production of sensors, lamps, solar cells, and high-resolution monitors for computers or mobile telephones.[1–5] Magnetic particles, on the other hand, are applied for immobilization, isolation, modification, and removal of biological active compounds.[6–10] Beyond these classical applications, the joining of magnetic and luminescent properties in one single assembly represents a significant step for biotechnological and medical applications such as biosensing, bioimaging, and DNA labeling.[11–13] Several examples of core–shell magnetic–fluorescent nanoparticles (NPs) have been reported previously in the literature.[14–23] In general, these particles are composed of a magnetic core combined with a coating layer of luminescent material.

The magnetic properties allow the manipulation of the NPs by applying a magnetic field as well as their easy separation from complex biological media. However, the magnetic core usually consists of transition-metal-based compounds such as magnetite (Fe_3O_4) or maghemite (γ-Fe_2O_3) NPs, which absorb light in the visible range, reducing the efficiency of the luminescent coating layer by means of the so-called killer effect.[24] This impasse is solved by building a protective layer of, for example, SiO_2 between the magnetic core and the luminescent shell.[14–19] Moreover, the coating layer is often composed of quantum dots,[25–28] or small luminescent molecules such as $[Ru(bpy)_3]^{2+}$ (bpy = 2′2′-bipyridine), usually embedded in a SiO_2 coating matrix. A major disadvantage of these materials is the emission of light only in parallel to the excitation process. In addition, quantum dots are often cadmium-based materials, and are, therefore, considerably toxic; for this reason, they are not ideal for biological applications,[29] similarly to $[Ru(bpy)_3]^{2+}$-containing materials. In contrast to fluorescent–magnetic NPs, afterglow materials are much more appropriate for bioimaging applications, as they offer a solution for the auto-fluorescence problem, in which fluorescent materials present in the living cells are excited in parallel with the marker.[30] For this reason, in the ideal case, the marker must emit light after the excitation light is blocked. Moreover, NPs showing persistent luminescence solve the problem that the penetration depth of tissues by visible radiation is low, so excitation of non-afterglow NPs in vivo is rather inefficient, whereas afterglow NPs can be excited with UV radiation even before injection.[31]

However, afterglow effects can be reached through more challenging mechanisms than fluorescence, requiring, for instance, a combination of lattice defects and energy transfer between mixed-valent lanthanide ions such as in $SrAl_2O_4:Eu^{2+},Dy^{3+}$.[32–34]

Strontium aluminate co-doped with Eu^{2+} and Dy^{3+} is a highly efficient afterglow material, developed in the 1990s by

[a] H. Terraschke, C. Wickleder
Inorganic Chemistry, Cμ—Center for Micro- and Nanochemistry and Engineering, Science and Technology Faculty
University of Siegen, Adolf-Reichwein-Str. 2, 57068 Siegen (Germany)
E-mail: wickleder@chemie.uni-siegen.de

[b] M. Franzreb
Institute of Functional Interfaces
Karlsruhe Institute of Technology, Hermann-von Helmholtz-Platz 1
76344 Eggenstein-Leopoldshafen (Germany)

[c] H. Terraschke
Current affiliation: Institut für Anorganische Chemie
Christian-Albrechts-Universität zu Kiel
Max-Eyth-Str. 2, 24118 Kiel (Germany)

Supporting information and the ORCID identification number(s) for the author(s) of this article can be found under: https://doi.org/10.1002/chem.201904551.

Matsuzawa et al.[35] and often reduced to the nanoscale applying the so-called combustion synthesis.[36–39] This method is usually applied for the preparation of highly crystalline compounds, for example, complex oxide ceramics such as silicates,[40] ferrites,[41] and chromites.[42] This process consists of an exothermic redox reaction of an oxidizer, for example, metal nitrates, and a reducing organic fuel such as urea.[43,44] Urea is reported to act additionally as a dispersive agent for the nanoparticles.[44]

In the present work, multifunctional double core–shell nanoparticles with magnetic and persistent luminescent behavior are presented for the first time, and have been registered recently in a patent process.[45] The development of the resulting Fe_3O_4@SiO_2@$SrAl_2O_4$:Eu^{2+},Dy^{3+} NPs (Scheme 1) represents a remarkable potential advance, for instance, for the detection of diagnostically relevant biomolecules or the marking and separation of cells in vitro. The intermediate SiO_2 layer is necessary to avoid quenching of the luminescence caused by the iron ions.

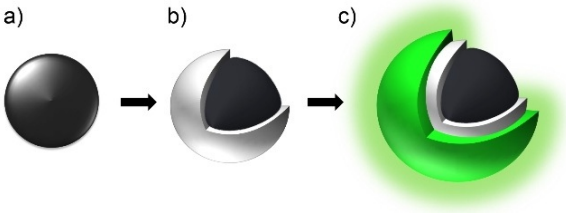

Scheme 1. Illustrative sketch of the composition of magnetic–afterglow particles containing a) Fe_3O_4 magnetic core (in black), b) SiO_2 protective layer (in gray), c) $SrAl_2O_4$:Eu^{2+},Dy^{3+} afterglow shell (in green).

Results and Discussion

The powder X-ray diffraction (XRD) results (Figure 1) demonstrate the successful preparation of each of the stage products for the synthesis of the Fe_3O_4@SiO_2@$SrAl_2O_4$:Eu^{2+},Dy^{3+} NPs, matching their expected calculated patterns.[46,47] Interestingly, the diffraction pattern of the Fe_3O_4@SiO_2 NPs does not differ from that measured for uncoated Fe_3O_4 particles. This is explained by the formation of an amorphous SiO_2 layer on the surface of the Fe_3O_4 material, which is not detectable by means of XRD analysis.[48] Therefore, the detailed analysis of the SiO_2 layer through energy-dispersive X-ray (EDX) investigations will be presented below. Comparing the XRD measurement of Fe_3O_4@SiO_2@$Sr_{0.97}Al_2O_4$:$Eu_{0.01}{}^{2+}$,$Dy_{0.02}{}^{3+}$ with the calculated XRD pattern for $SrAl_2O_4$,[47] no shift on the single reflexes is observed, indicating that there was no variation in the dimension of the unit cell despite the introduction of the Eu^{2+} and Dy^{3+} ions. In addition, the broad reflexes and low crystallinity detected by means of the measured diffraction patterns are expected because of the low dimension of the nanosized crystals.

The nanoscale dimensions of the synthesized Fe_3O_4, Fe_3O_4@SiO_2, and Fe_3O_4@SiO_2@$SrAl_2O_4$:Eu^{2+},Dy^{3+} particles were confirmed by AFM and SEM, shown in Figures S1 and S2, respectively (Supporting Information). According to the section analysis of the respective AFM images, the size of the magnetic NPs increased from approximately 15 nm for bare Fe_3O_4 NPs (Figure S1 a) to around 47 nm after coating with the SiO_2 protective layer (Figure S1 b). After additional coating with the afterglow $SrAl_2O_4$:Eu^{2+},Dy^{3+} shell, the size of the nanoparticles increased to approximately 67 nm (Figure S1 c).

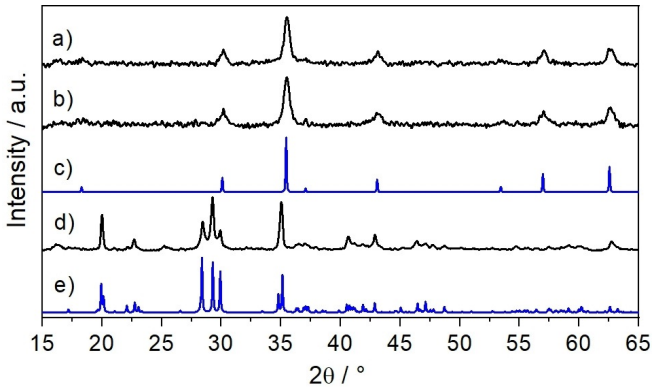

Figure 1. X-ray diffraction analysis of synthesized a) Fe_3O_4 NPs and b) Fe_3O_4@SiO_2 NPs, in comparison with c) the calculated diffraction pattern of Fe_3O_4. d) XRD measurement of synthesized Fe_3O_4@SiO_2@$Sr_{0.97}Al_2O_4$:$Eu_{0.01}{}^{2+}$,$Dy_{0.02}{}^{3+}$ NPs, in comparison with calculated pattern of $SrAl_2O_4$.

Figure S2 shows SEM images of different stages of the preparation of the magnetic–afterglow NPs. These images confirm the nanosized diameter of the uncoated and coated particles as well as their spherical morphology. Moreover, EDX spectroscopy was used in combination with the SEM analysis to confirm the formation of the coating layers on the surface of the magnetic core. As explained above, the EDX analysis was especially important for verifying the formation of the SiO_2 protective layer, as it could not be detected by XRD measurements owing to its amorphous nature.[48] As displayed in Figure 2 a, the chemical composition of the uncoated NPs shows only signals related to the Fe_3O_4 core, whereas the analogous measurement of the Fe_3O_4@SiO_2 NPs clearly exhibits signals assigned not only to the iron but also to the silicon content (Figure 2 b), indicating the successful formation of the SiO_2 layer. Similarly, EDX measurements of the magnetic NPs coated with the co-doped strontium aluminate shell also confirmed the presence of strontium, aluminum, europium, dysprosium, and iron in the chemical composition of the magnetic afterglow NPs (Figure 2 c,d). The overlap between the signals assigned to silicon, strontium, and aluminum probably prevented the detection of the Si content in Figure 5 c.

Under daylight, the voluminous Fe_3O_4@SiO_2@$SrAl_2O_4$:Eu^{3+},Dy^{3+} formed from the Sr, Al, Eu, and Dy nitrate precursors for the combustion synthesis and the magnetic NPs is rather colorless, slightly darkened owing to the involved Fe_3O_4@SiO_2 particles (Figure 3 a). Upon irradiation with UV light, this sample emits reddish light (Figure 3 b), characteristic of the electronic transitions of the europium ions in the trivalent oxidation states. After annealing under a reducing atmosphere of H_2/Ar, the resulting Fe_3O_4@SiO_2@$SrAl_2O_4$:Eu^{2+},Dy^{3+} nanosized powder (Figure 3 c) emits green light upon UV radiation, assigned to

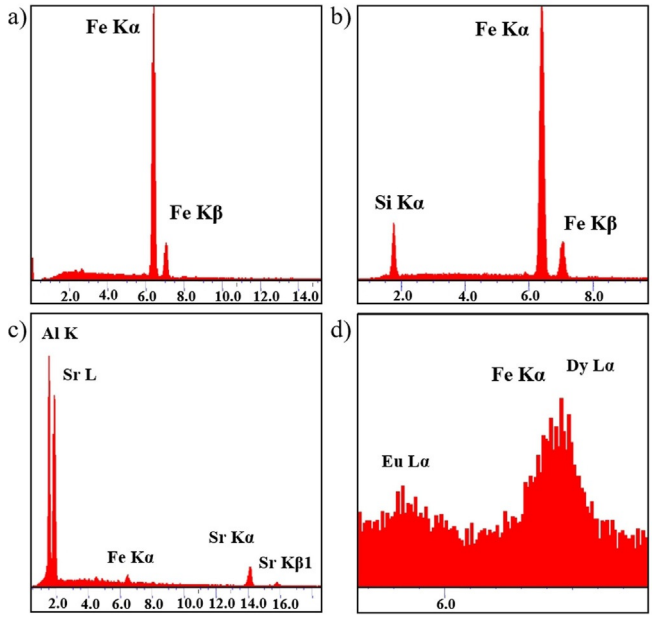

Figure 2. Energy-dispersive X-ray spectroscopic analysis of a) uncoated Fe_3O_4 NPs, b) Fe_3O_4@SiO_2, c, d) Fe_3O_4@SiO_2@$SrAl_2O_4$:Eu^{2+},Dy^{3+} NPs.

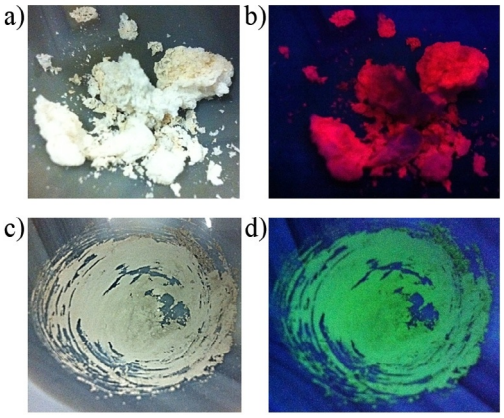

Figure 3. Voluminous Fe_3O_4@SiO_2@$SrAl_2O_4$:Eu^{3+},Dy^{3+} after combustion synthesis, irradiated with a) daylight and b) UV light. Fe_3O_4@SiO_2@$SrAl_2O_4$:Eu^{2+},Dy^{3+}, after sintering under reductive atmosphere, irradiated with c) daylight and d) UV light.

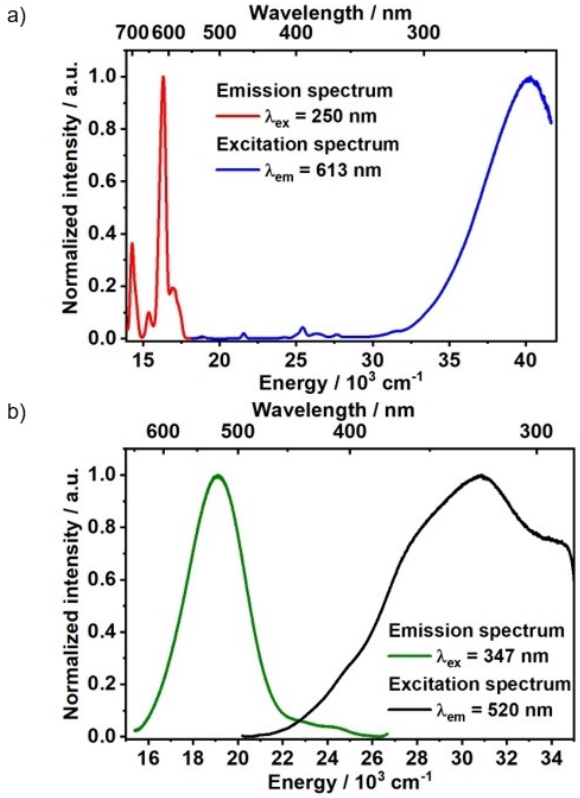

Figure 4. a) Emission (λ_{ex} = 250 nm, red curve) and excitation (λ_{em} = 613 nm, blue curve) spectra of Fe_3O_4@SiO_2@$SrAl_2O_4$:Eu^{3+},Dy^{3+} after the combustion synthesis. b) Emission (λ_{ex} = 347 nm, green curve) and excitation (λ_{em} = 520 nm, black curve) spectra of Fe_3O_4@SiO_2@$SrAl_2O_4$:Eu^{2+},Dy^{3+} NPs after the post-synthetic reducing step.

the electronic transitions of the divalent europium ions (Figure 3 d).

In accordance with the red luminescence of Fe_3O_4@SiO_2@$SrAl_2O_4$:Eu^{3+},Dy^{3+} after the combustion synthesis, the emission spectrum of these samples consists of several peaks distributed mostly over the red spectral range (Figure 4 a, red curve). These peaks present very broad features owing to a combination of three main factors. The first factor is the overlap of the emission peaks attributed to the $^5D_0 \rightarrow {}^7F_0$ transitions of Eu^{3+} and $^4F_{9/2} \rightarrow {}^6H_{11/2-13/2}$ transitions of Dy^{3+} (Figure S3, Supporting Information).[49] Secondly, the overall emission spectrum of Fe_3O_4@SiO_2@$SrAl_2O_4$:Eu^{3+},Dy^{3+} can be also broadened by the overlap of the single spectral lines assigned to the 4f→4f electronic transition of the Eu^{3+} and Dy^{3+} ions doping each of the strontium crystallographic sites in $SrAl_2O_4$.[47] Lastly, distortions and defects in the nanoparticles and the large surface also cause slightly different coordination spheres of the Eu^{3+} ions. Therefore, the emission peaks assigned to the 4f→4f electronic transitions are additionally broad, and no crystal field splitting effect could be observed, which is the general case for nanoparticles doped with trivalent lanthanides.[40] Among the Eu^{3+} transitions within the emission spectrum of Fe_3O_4@SiO_2@$SrAl_2O_4$:Eu^{3+},Dy^{3+}, the transition assigned to $^5D_0 \rightarrow {}^7F_2$ at 16297 cm^{-1} is the most intense one because of the low point symmetry of the Eu^{3+} site. Even though the Dy^{3+} concentration is higher than that of Eu^{3+}, the emission intensity assigned to the Dy^{3+} transitions is lower than that assigned to Eu^{3+}, probably owing to the energy transfer between the $^4F_{9/2}$ level of Dy^{3+} and the $^5D_0$ level of Eu^{3+}.[50] The excitation spectrum of Fe_3O_4@SiO_2@$SrAl_2O_4$:Eu^{3+},Dy^{3+} is composed of a broad band distributed from about 30000 cm^{-1} with a maximum at around 40000 cm^{-1} (Figure 4 a, blue curve). This behavior of the excitation spectrum of Fe_3O_4@SiO_2@$SrAl_2O_4$:Eu^{3+},Dy^{3+} agrees with that reported for $SrAl_2O_4$:Eu^{3+} by Sahu et al.,[51] in which the excitation band at approximately 39000 cm^{-1} is assigned to the charge-transfer state (CTS) caused by the electron transfer from an oxygen 2p orbital to an empty 4f shell of europium. This broad band largely overcomes the peaks between 18000 and 32000 cm^{-1}, which origi-

nate from the electronic transitions of trivalent europium, indicating an efficient energy-transfer process between the CT state and the $^5D_0 \rightarrow {}^7F_J$ transitions of Eu^{3+}.[51]

After sintering under an Ar/H_2 atmosphere, Eu^{3+} ions are reduced to their divalent oxidation state. In the respective emission spectrum, a main broad band is observed, located at 19230 cm^{-1} (520 nm) with a full-width at half-maximum (FWHM) of 2947 cm^{-1}, accompanied by two bands of lower intensity at 24400 cm^{-1} (410 nm) and 23000 cm^{-1} (435 nm) (Figure 4b, green curve). According to our previous work,[33] the green band at 520 nm is attributed to delocalization of the excited electron into the conduction band, thus leading to the formation of an impurity-trapped exciton at Eu^{2+}. Both bands in the blue spectral range at 410 and 435 nm, on the other hand, are assigned to the $4f^65d^1 \rightarrow 4f^7$ ($^8S_{7/2}$) transition of Eu^{2+} within both the available Sr^{2+} crystallographic sites in the strontium aluminate host lattice.[47] Within this spectrum, even though no 4f→4f electronic transition of Dy^{3+} is detected, the presence of the Dy^{3+} ions is necessary for the generation of the afterglow effect.[33] The resulting $Fe_3O_4@SiO_2@SrAl_2O_4:Eu^{2+},Dy^{3+}$ NPs are then able to emit light for few seconds after the source of excitation energy is turned off. This luminescence intensity and afterglow effect are, however, weaker than those detected for pure $SrAl_2O_4:Eu^{2+},Dy^{3+}$ NPs, which can emit light for several minutes after the extinction of the excitation light source (Figure 5).[20] The respective excitation spectra are widely spread over the UV and part of the visible range of the electromagnetic spectrum, starting at about 21000 cm^{-1}, with a maximum at 30820 cm^{-1} (Figure 4b, black curve), similarly to that previously reported for $SrAl_2O_4:Eu^{2+}$ nanoparticles.[33]

The synthesized Fe_3O_4 NPs are highly magnetizable and can be separated easily from solutions by a magnetic field (Figure 6a). Similarly, the resulting $Fe_3O_4@SiO_2@SrAl_2O_4:Eu^{2+},Dy^{3+}$ NPs are still magnetizable despite the isolating nature of the coating layers, and show green luminescence during and for a few seconds after irradiation with UV light (Figure 6b).

In general, it is important to mention that the thickness of the SiO_2 and $SrAl_2O_4$ layers can be modified by adjusting the appropriated synthesis parameters. For instance, the thickness of the SiO_2 layer can be increased by enhancing the concentration of the respective tetraethyl orthosilicate precursor in the corresponding coating solution or increasing the reaction time. On the other hand, the thickness of the afterglow $SrAl_2O_4:Eu^{2+},Dy^{3+}$ layer can be reduced by increasing the concentration of $Fe_3O_4@SiO_2$ NPs for the combustion synthesis. However, the formation of the coating layers reduces the magnetizability of the Fe_3O_4 core, owing to the isolator character of SiO_2 and $SrAl_2O_4:Eu^{2+},Dy^{3+}$. In contrast, despite the formation of the SiO_2 protective layer, the magnetic core partially quenches the luminescence of the $SrAl_2O_4:Eu^{2+},Dy^{3+}$ shell. For these reasons, the ratio between the size of the magnetic core and the applied coating shells is a very important parameter for assuring the bifunctionality and the respective efficiencies of both functionalities. The object of this paper is, however, to introduce these respective bifunctional nanoparticles; efforts to improve their efficiency by varying the thickness of the core and the shells together with detailed measurements of the persistent luminescence will be described in another paper.

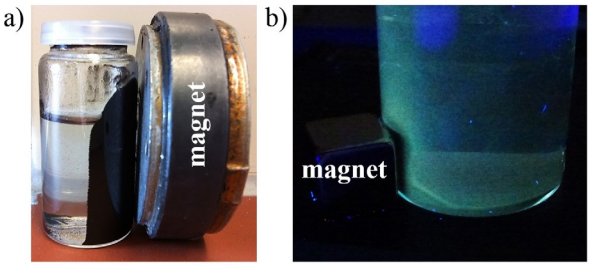

Figure 6. a) Uncoated Fe_3O_4 NPs attracted by a magnetic field. b) Magnetic–afterglow $Fe_3O_4@SiO_2@SrAl_2O_4:Eu^{2+},Dy^{3+}$ NPs separated from an ethanolic suspension by a magnetic field, under UV light irradiation.

Conclusions

This work presents a double core–shell strategy for the synthesis of novel magnetic–afterglow NPs. The particles were synthesized by combining precipitation and combustion synthesis routes. Hence, the core of this bifunctional nanocomposite consists of Fe_3O_4 NPs, which are coated by a protective SiO_2 middle layer, itself covered by an afterglow $SrAl_2O_4:Eu^{2+},Dy^{3+}$ shell. According to AFM measurements, the size of the Fe_3O_4 core is around 15 nm, increasing to approximately 47 nm after the SiO_2 coating and to around 67 nm after the formation of the co-doped strontium aluminate shell. The compositions of the core and both shells were confirmed by XRD analysis and EDX spectroscopy. Directly after the combustion synthesis, the $Fe_3O_4@SiO_2@SrAl_2O_4:Eu^{3+},Dy^{3+}$ NPs present red luminescence upon irradiation with UV light, in accordance with the $^5D_0 \rightarrow {}^7F_J$ ($J = 0$–4) transitions identified in the respective emission

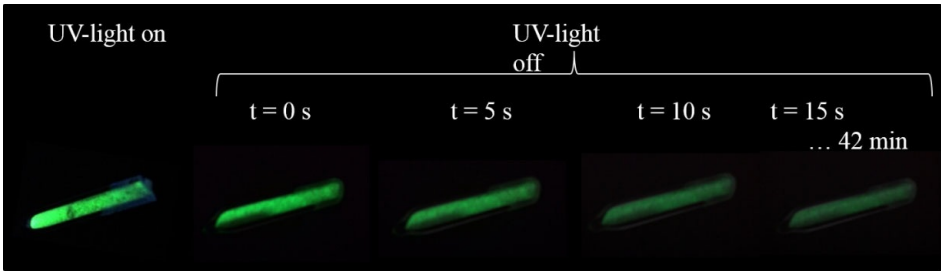

Figure 5. Emission of $SrAl_2O_4:Eu^{2+},Dy^{3+}$ nanoparticles during irradiation with UV light (left) and up to 42 min after the UV light source was turned off. Reproduced with permission from reference [20].

spectrum. After the post-synthetic reducing step, the Fe_3O_4@SiO_2@$SrAl_2O_4$:Eu^{2+},Dy^{3+} NPs emit green light during and for a few seconds after excitation with UV radiation. The respective emission spectrum presents a main emission band at 19230 cm^{-1}, assigned to the $4f^65d^1 \rightarrow 4f^7$ ($^8S_{7/2}$) transition of Eu^{2+} in strontium aluminate. Despite the isolating nature of the coating layer and the quenching effect of the iron oxide core, the synthesized NPs are magnetizable, and show not only fluorescent but also afterglow effects. Such bifunctional composites can be applied, for instance, as markers for the identification of cancer cells, for the detection of diagnostically relevant biomolecules, or for the marking and separation of cells in vitro.

Experimental Section

All reagents were purchased from commercial sources and used without further purification. The applied method for the preparation and coating of the plain magnetic iron oxide NPs is based on the work of Zhang et al.[17] In summary, for the synthesis of the magnetic Fe_3O_4 core, a 1 M aqueous solution of $FeCl_3 \cdot 6H_2O$ (50 mL; Alfa Aesar, Karlsruhe, Germany, 98%) was mixed with a weak acidic aqueous solution of $FeCl_2 \cdot 4H_2O$ (Alfa Aesar, 98%). Afterwards, the mixture was added to 0.7 M ammonia solution (500 mL; Sigma–Aldrich, 26%) in water under a N_2 atmosphere, causing the immediate precipitation of the Fe_3O_4 NPs, which were finally washed with water and dried at 75 °C for 3 h. A SiO_2 coat was built by suspending the freshly prepared Fe_3O_4 core in a solution of NH_4OH (3 mL) in water (28.8 mL) and ethanol (27.5 mL), dropping it into a solution of tetraethyl orthosilicate (1.5 mL; TEOS, Alfa Aesar, 98%) in ethanol (30 mL). The solution was stirred for 2 h, washed with ethanol, and dried at 75 °C for a further 3 h.

As explained above, the $SrAl_2O_4$:Eu^{2+},Dy^{3+} luminescent layer was produced through the so-called combustion method. For this purpose, the magnetic particles were added to stoichiometric amounts of $Sr(NO_3)_2$ (Merck Chemicals, Darmstadt, Germany), $Al(NO_3)_3 \cdot 9H_2O$, $Eu(NO_3)_3 \cdot 6H_2O$ (1 mol%, Chempur, Karlsruhe, Germany, 99.9%), and $Dy(NO_3)_3 \cdot 5H_2O$ (2 mol%, Alfa Aesar, 99.9%), mixed with distilled water together with 20 times molar excess of NH_2CONH_2 (Alfa Aesar, 99+%), and heated to 600 °C. At this temperature, the water evaporates, the metal nitrates decompose, and a spontaneous ignition is caused by the urea content, forming a voluminous $SrAl_2O_4$:Eu^{3+},Dy^{3+} product, which involves the Fe_3O_4 core. Afterglow effects were achieved by annealing the product from the combustion synthesis at 1100 °C under an Ar/H_2 atmosphere, which was responsible for reducing Eu^{3+} to Eu^{2+}.

Photoluminescence investigations of the solid samples in silica ampoules were performed with a Fluorolog3 spectrofluorometer FI3-22 (Horiba Jobin Yvon, Longjumeau, France) equipped with double Czerny–Turner monochromators, a 450 W xenon lamp, and an R928P photomultiplier (Hamamatsu, Herrsching, Germany) with a photon-counting system. All emission spectra were corrected for photomultiplier sensitivity, the excitation spectra for lamp intensity, and both for the transmission of the monochromators. Powder X-ray diffraction was measured on a D5000 X-ray diffractometer (Siemens, Karlsruhe, Germany) operating at 40 kV, 30 mA with CuK_α radiation ($\lambda = 0.154178$ nm). Microscopy investigations were performed on a CS44 scanning electron microscope (SEM, CamScan, Cambridge, UK), equipped with energy-dispersive X-ray spectroscopy (EDAX, Mahwah, USA) and on an atomic force microscope (AFM) Multimode 2, applying an AC200TS cantilever.

Conflict of interest

The authors declare no conflict of interest.

Keywords: afterglow · combustion synthesis · luminescence · magnetism · nanoparticles

[1] W. M. Yen, S. Shionoya, H. Yamamoto, *Phosphor Handbook*, CRC/Taylor and Francis, Boca Raton, **2007**.
[2] M. J. Li, Z. Chen, V. W. W. Yam, Y. Zu, *ACS Nano* **2008**, *2*, 905–912.
[3] L. Zhang, B. Liu, S. Dong, *J. Phys. Chem. B* **2007**, *111*, 10448–10452.
[4] M. Bottrill, M. Green, *Chem. Commun.* **2011**, *47*, 7039–7050.
[5] F. Yoshimura, K. Nakamura, F. Wakai, M. Hara, M. Yoshimoto, O. Odawara, H. Wada, *Appl. Surf. Sci.* **2011**, *257*, 2170–2175.
[6] T. Maldiney, A. Bessière, J. Seguin, E. Teston, S. K. Sharma, B. Viana, A. J. J. Bos, P. Dorenbos, M. Bessodes, D. Gourier, D. Scherman, C. Richard, *Nat. Mater.* **2014**, *13*, 418–426.
[7] T. Matsuzawa, Y. Aoki, N. Takeuchi, Y. Murayama, *J. Electrochem. Soc.* **1996**, *143*, 2670–2673.
[8] H. C. Streit, J. Kramer, M. Suta, C. Wickleder, *Materials* **2013**, *6*, 3079–3093.
[9] A. B. Salunkhe, V. M. Khot, M. R. Phadatare, S. H. Pawar, *J. Alloys Compd.* **2012**, *514*, 91–96.
[10] S. S. Manoharan, K. C. Patil, *J. Am. Ceram. Soc.* **1992**, *75*, 1012–1015.
[11] Y. Zheng, D. Chen, *Luminescence* **2011**, *26*, 481–485.
[12] I. Gonzalo-Juan, B. Ferrari, M. T. Colomer, *J. Eur. Ceram. Soc.* **2009**, *29*, 3185–3195.
[13] M. Franzreb, H. C. Streit, C. Wickleder.Germany Patent 102013022052.1, 23.12, **2013**.
[14] N. Tombs, *Acta Crystallogr.* **1951**, *4*, 474–475.
[15] A. R. Schulze, H. Müller Buschbaum, *Z. Anorg. Allg. Chem.* **1981**, *475*, 205–210.
[16] C. Hui, C. Shen, J. Tian, L. Bao, H. Ding, C. Li, Y. Tian, X. Shi, H. J. Gao, *Nanoscale* **2011**, *3*, 701–705.
[17] G. H. Dieke, *Spectra and Energy Levels of RE Ions in Crystals*, Wiley, New York, **1968**.
[18] A. N. Meza-Rocha, A. Speghini, M. Bettinelli, U. Caldiño, *J. Lumin.* **2016**, *176*, 235–239.
[19] I. P. Sahu, D. P. Bisen, N. Brahme, R. K. Tamrakar, *J. Mater. Sci. Mater. Electron.* **2016**, *27*, 3443–3455.
[20] H. Terraschke, M. Suta, M. Adlung, S. Mammadova, N. Musayeva, R. Jabbarov, M. Nazarov, C. Wickleder, *J. Spectrosc.* **2015**, 541958.
[21] D. Przybylska, A. Ekner-Grzyb, B. F. Grześkowiak, T. Grzyb, *Sci. Rep.* **2019**, *9*, 8669.
[22] T. Cesca, G. Perotto, G. Pellegrini, N. Michieli, B. Kalinic, G. Mattei, *Sci. Rep.* **2018**, *8*, 13811.
[23] L. Bischoff, M. Stephan, C. S. Birkel, C. F. Litterscheid, A. Dreizler, B. Albert, *Sci. Rep.* **2018**, *8*, 602.
[24] M. Franzreb, M. Siemann-Herzberg, T. J. Hobley, O. R. T. Thomas, *Appl. Microbiol. Biotechnol.* **2006**, *70*, 505–516.
[25] S. Berensmeier, *Appl. Microbiol. Biotechnol.* **2006**, *73*, 495–504.
[26] X. Yan, Q. Zhou, M. Vincent, Y. Deng, J. Yu, J. Xu, T. Xu, T. Tang, L. Bian, Y.-X. J. Wang, K. Kostarelos, L. Zhang, *Sci. Robot.* **2017**, *2*, eaaq1155.
[27] Y. Zhang, L. Zhang, L. Yang, C. I. Vong, K. F. Chan, W. K. K. Wu, T. N. Y. Kwong, N. W. S. Lo, M. Ip, S. H. Wong, J. J. Y. Sung, P. W. Y. Chiu, L. Zhang, *Sci. Adv.* **2019**, *5*, 9650.
[28] H. Terraschke, M. Rothe, A.-M. Tsirigoni, P. Lindenberg, L. Ruiz Arana, N. Heidenreich, F. Bertram, M. Etter, *Inorg. Chem. Front.* **2016**, *3*, 1157–1165.
[29] P. Polzin, I. V. Eliani, J. Ströh, M. Braun, N. Ruser, N. Heidenreich, P. Rönfeldt, F. Bertram, M. Suta, H. Terraschke, unpublished results.
[30] Q. Yu, Y.-M. Zhang, Y.-H. Liu, X. Xu, Y. Liu, *Sci. Adv.* **2018**, *4*, eaat2297.
[31] Q. Chang, L. Zhu, C. Yu, H. Tang, *J. Lumin.* **2008**, *128*, 1890–1895.
[32] C. W. Lai, Y. H. Wang, C. H. Lai, M. J. Yang, C. Y. Chen, P. T. Chou, C. S. Chan, Y. Chi, Y. C. Chen, J. K. Hsiao, *Small* **2008**, *4*, 218–224.
[33] J. Choi, J. C. Kim, Y. B. Lee, I. S. Kim, Y. K. Parka, N. H. Hur, *Chem. Commun.* **2007**, 1644–1646.

[34] F. Zhang, G. B. Braun, A. Pallaoro, Y. Zhang, Y. Shi, D. Cui, M. Moskovits, D. Zhao, G. D. Stuck, *Nano Lett.* **2012**, *12*, 61 – 67.
[35] L. U. Khan, G. H. da Silva, A. M. Z. de Medeiros, Z. U. Khan, M. Gidlund, H. F. Brito, O. Moscoso-Londoño, D. Muraca, M. Knobel, C. A. Pérez, D. S. T. Martinez, *ACS Appl. Nano Mater.* **2019**, *2*, 3414 – 3425.
[36] D. Wang, J. He, N. Rosenzweig, Z. Rosenzweig, *Nano Lett.* **2004**, *4*, 409 – 413.
[37] V. Salgueiriño-Maceira, M. A. Correa-Duarte, M. Spasova, L. M. Liz-Marzán, M. Farle, *Adv. Funct. Mater.* **2006**, *16*, 509 – 514.
[38] X. Hong, J. Li, M. Wang, J. Xu, W. Guo, J. Li, Y. Bai, T. Li, *Chem. Mater.* **2004**, *16*, 4022 – 4027.
[39] R. Di Corato, N. C. Bigall, A. Ragusa, D. Dorfs, A. Genovese, R. Marotta, L. Manna, T. Pellegrino, *ACS Nano* **2011**, *5*, 1109 – 1121.
[40] H. Terraschke, C. Wickleder, *Chem. Rev.* **2015**, *115*, 11352.
[41] K. Van den Eeckhout, P. F. Smet, D. Poelman, *Materials* **2010**, *3*, 2536 – 2566.
[42] R. E. Rojas-Hernandez, F. Rubio-Marcos, M. A. Rodriguez, J. F. Fernandez, *Renewable Sustainable Energy Rev.* **2018**, *81*, 2759 – 2770, and references therein.
[43] M. Nazarov, M. G. Brik, D. Spassky, B. Tsukerblat, *J. Lumin.* **2017**, *182*, 79 – 86.
[44] M. L. Chithambo, A. H. Wako, A. A. Finch, *Radiat. Meas.* **2017**, *97*, 1 – 13.
[45] V. Chernov, P. Salas-Castillo, L. Díaz-Torres, N. J. Zúñiga-Rivera, R. Ruiz-Torres, R. Meléndreza, M. Barboza-Flores, *Opt. Mater.* **2019**, *92*, 46 – 52.
[46] Z. Y. Ma, D. Dosev, M. Nichkova, S. J. Gee, B. D. Hammock, I. M. Kennedy, *J. Mater. Chem.* **2009**, *19*, 4695 – 4700.
[47] C. Mi, J. Zhang, H. Gao, X. Wu, M. Wang, Y. Wu, Y. Di, Z. Xu, C. Mao, S. Xu, *Nanoscale* **2010**, *2*, 1141 – 1148.
[48] M. Nichkova, D. Dosev, S. J. Gee, B. D. Hammock, I. M. Kennedy, *Anal. Biochem.* **2007**, *369*, 34 – 40.
[49] L. Wang, Z. Yang, Y. Zhang, L. Wang, *J. Phys. Chem. C* **2009**, *113*, 3955 – 3959.
[50] R. Amin, A. Khorshidi, A. F. Shojaei, S. Rezaei, M. A. Faramarzi, *Int. J. Biol. Macromol.* **2018**, *114*, 106 – 113.
[51] D. K. Deda, R. M. Cardoso, M. K. Uchiyama, C. Pavani, S. H. Toma, M. S. Baptista, K. Araki, *Anal. Bioanal. Chem.* **2017**, *409*, 6663 – 6675.

Manuscript received: October 4, 2019
Revised manuscript received: December 14, 2019
Accepted manuscript online: January 10, 2020
Version of record online: April 30, 2020

